PASSIVATION OF INSB INFRARED PHOTODETECTORS

A THESIS

SUBMITTED TO THE DEPARTMENT OF PHYSICS

AND THE INSTITUTE OF ENGINEERING AND SCIENCE

OF BILKENT UNIVERSITY

IN PARTIAL FULFILLMENT OF THE REQUIREMENTS

FOR THE DEGREE OF

MASTER OF SCIENCE

By

Samed Yumrukçu

July, 2010

I certify that I have read this thesis and that in my opinion it is fully adequate, in scope and in quality, as a thesis for the degree of Master of Science.

Prof. Dr. Atilla Aydınlı(Advisor)

I certify that I have read this thesis and that in my opinion it is fully adequate, in scope and in quality, as a thesis for the degree of Master of Science.

Prof. Dr. Raşit Turan

I certify that I have read this thesis and that in my opinion it is fully adequate, in scope and in quality, as a thesis for the degree of Master of Science.

Assoc. Prof. Dr. Ceyhun Bulutay

Approved for the Institute of Engineering and Science:

Prof. Dr. Levent Onural
Director of the Institute

ABSTRACT

PASSIVATION OF INSB INFRARED PHOTODETECTORS

Samed Yumrukçu
M.S. in Physics
Supervisor: Prof. Dr. Atilla Aydınlı
July, 2010

Infrared detectors have wide range applications in both military and civilian life. One of the most commonly used infrared detectors is InSb detectors. InSb detector technology has been developing since 1950s. Fabricating p-n diodes to detect infrared radiation is a common way of constructing InSb detectors. Due to high free carrier concentration at room temperature, InSb detectors need to be cooled down to operate properly and usually liquid nitrogen is preferred for cooling. However, even at 77 K, tunneling and generation-recombination and surface leakage are not negligible and these effects result in dark current. Improving the photo current-to-dark current ratio is the main goal in design and fabrication of InSb photo detectors. One way of decreasing the dark current is passivating the exposed edges of the detector to reduce surface leakage current. Passivating the edges can result in decreasing in the surface leakage by eliminating the surface states (dangling bonds). Dielectric thin films like SiO_2 and SiN_x are commonly used for passivation. In this work, different sized detectors are fabricated and characterized by measuring I-V curves and spectral response. Different approaches are tested for passivation and a detailed comparison between detectors with different treatments is presented.

Keywords: InSb, Photo detectors, Passivation, Infrared Radiation.

ÖZET

INSB KIZILÖTESİ DETEKTÖRLERİN PASİFLEŞTİRİLMESİ

Samed Yumrukçu
Fizik, Yüksek Lisans
Tez Yöneticisi: Prof. Dr. Atilla Aydınlı
Temmuz, 2010

Kızılötesi dedektörler hem askeri hem de sivil alanda çok geniş uygulamalara sahiptir. En çok kullanılan dedektör çeşitlerinden bir tanesi InSb dedektörlerdir. InSb dedektör teknolojisi 1950lerden beri gelişimini sürdürmektedir. InSb dedektör üretiminde en çok kullanılan yöntemlerden biri de p-n diyot yapımıdır. Oda sıcaklığında yüksek serbest taşıyıcı yoğunluğuna sahip olan InSb dedektörler etkili çalışabilmeleri için soğutulmalıdırlar, soğutma için tercihen sıvı azot kullanılır. 77 K sıcaklığa rağmen, tünelleme, üretme-tüketme ve yüzey kaçağı etkileri karanlık akıma neden olmaktadır. Sinyal / Karanlık akım oranının iyileştirilmesi ana amaçtır. Karanlık akımı azaltmanın yollarından biri de dedektör kenarlarının pasifleştirilmesidir. Kenarların pasifleştirilmesi yüzey durumlarını (asılı bağlar) bertaraf ederek yüzey kaçağında azalmaya sebep olur. Pasifleştirme işleminde genellikle SiO_2 ve SiN_x gibi yalıtkan filmler kullanılmaktadır. Bu tez çalışmasında, değişik boyutlarda dedektörlerin üretilmesi, akım-voltaj ve tayf tepkisi ölçümleri yapılmıştır. Pasifleştirme için değişik malzemeler kullanılmış ve bu değişik işlemlerin sonuçlarının detaylı bir karşılaştırması sunulmuştur.

Anahtar sözcükler: InSb, Işık dedektörü, Pasifleştirme, Kızılötesi Radyasyon.

Anneme ve Babama

to my parents ...

Acknowledgement

I would like to express my indebtedness to my academic supervisor Prof. Atilla Aydınlı for his encouragement and guidance.

I would like to thank Dr. Ömer Salihoğlu for teaching his experience in laboratory and helping me in my experiments.

I would like to thank to Kutlu Kutluer for his helps in my spectral response measurements at METU.

I would also like to thank my thesis committee, Prof. Dr. Raşit Turan and Assoc. Prof. Dr. Ceyhun Bulutay for their reading and commenting on this thesis.

I would like to thank my group mates Ertuğrul Karademir, Mustafa Karabıyık and Bektaş Akyazı for valuable discussions and their friendships.

I am indebted to Tuncay Özel, Seçkin Şenlik (aka 2 + 1) and Hasan Esat Kondakçı, Özge Özel, Ahmet Keleş, Cem Murat Turgut for their friendships and support during my eight years in Bilkent. Their friendship is invaluable for me. I will always remember the unforgettable poker nights.

I wish to express my special thanks to my parents and my brother Semih for their support and love.

I wish to express my deepest gratitude to my love, Şeyda İpek for always being next to me. Without her support, encouragement and love, this work would have been impossible.

The financial support from TÜBİTAK (Project no: 106M549) and ASELSAN for buying the InSb wafer are gratefully acknowledged.

Contents

List of Figures

Chapter 1

Introduction

Considering the wide range of wavelengths of the electromagnetic spectrum, detection of electromagnetic radiation has always been a challenge. Many types and kinds of detectors have been demonstrated and some are used commercially in specific parts of the spectrum, namely ultraviolet, visible and the infrared. Even in the case of available detectors the challenges continue to be to lower the cost, increase the speed and sensitivity and to build planar arrays that replace the photographic plate. In this context, detection of infrared radiation has wide range of applications in both military and civilian life: noncontact temperature measurements or detection of exhaust plumes from missiles and aircraft when they can not be seen by the naked eye as well as astronomical observations in the infrared.

This chapter introduces the infrared detection and detector types (MCT, QWIP, SL, and InSb) developed to detect it, in historical order. Detection mechanisms and figures of merits will be discussed.

1.1 Infrared Radiation

Infrared radiation was discovered by Herschel at the beginning of 1800. He constructed an experiment such that the sun light was monochromatized by a prism and using a pinhole, he was able to choose different colors. First, he discovered that different colors cause different temperature changes on the thermometer, and then he found that even when no visible light comes out of the pinhole, temperature on the thermometer still rises. As in his own words, he wrote: *thermometer no.* 1 *rose* 7 *degrees in* 10 *minutes by an exposure to the full red coloured rays. I drew back the stand... thermometer no.* 1 *rose, in* 16 *minutes* $8\frac{3}{8}$ *degrees when its centre was* $\frac{1}{2}$ *inch out of the visible rays.* [4]

After Herschel, thermal detectors were built based on heat detection. One of them is Langley's bolometer of 1880. A bolometer senses heat as the resistance of its components change due to temperature of the target. He used a platinum foil to construct a Wheatstone bridge to measure the changes in the resistance and he continued to develop his thermal detector for 20 years. His latest detector could sense a cow at a distance of quarter of a mile. [5]

As knowledge on light improved with quantum physics, it was discovered that all objects with temperature above 0 K emit radiation. However, photons emitted by human body are not visible to human eye due to relatively low temperatures involved. As the temperature of the object increases, radiation shifts towards the visible region. Thanks to Max Planck, we now describe the radiation emitted by hot objects in terms of the concept of blackbody. A blackbody is any object that absorbs all radiation falling onto it, reflects none and emits this energy with perfect efficiency. The temperature and wavelength dependence of this radiation is expressed by Planck's Law as shown in Fig. 1.1. Planck formulated the distribution of total radiated energy with respect to the wavelength of radiation.

Planck's Law $\rightarrow$

$$W(\lambda, T) = \frac{2\pi hc^2}{\lambda^5} \frac{1}{e^{\frac{hc}{\lambda kT}} - 1} \tag{1.1}$$

Here λ is in μm, T is in Kelvin. Wien calculated the peak wavelength of this radiation as:

Wien's Law $\rightarrow$

$$\lambda_{(max)} = \frac{2898}{T} \tag{1.2}$$

Stefan-Boltzmann law indicates the total radiated power in terms of temperature.

Stefan-Boltzmann Law $\rightarrow$

$$M = \sigma T^4 \tag{1.3}$$

Here σ is in $Wm^{-2}K^4$ and T is in Kelvin.

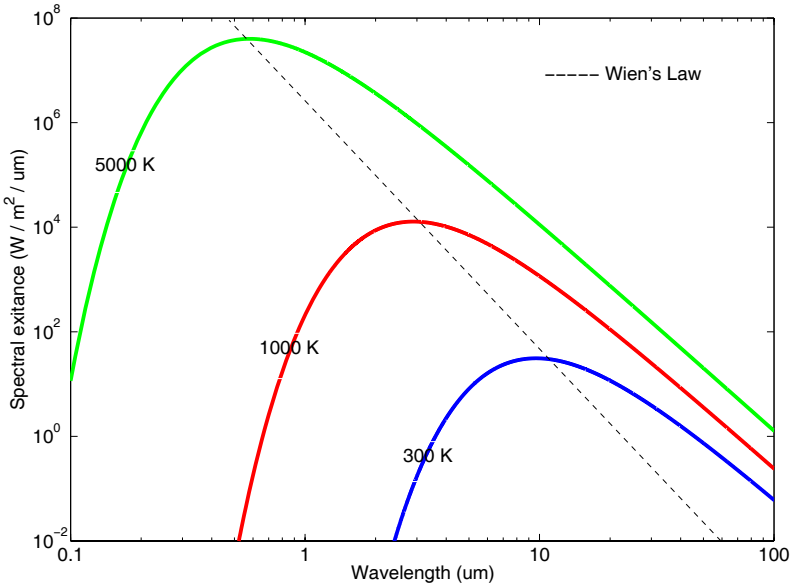

Figure 1.1: Planck's law for different temperatures, dashed line shows the peak wavelength according to Wien's law

As radiation propagates in air, different wavelengths of the radiation is absorbed or scattered by different components of air (CO_2, O_2, Ozone, CO, H_2O). Transmission spectrum of air is well known and is given below in Fig. 1.2

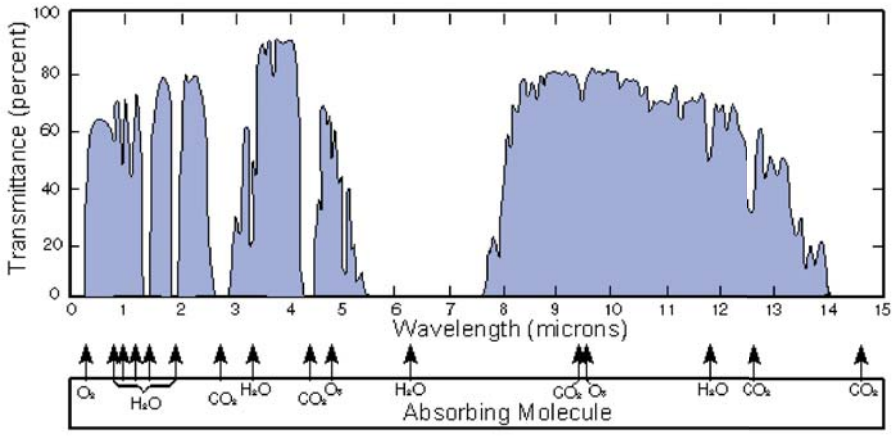

Figure 1.2: Transmission of light in air [free license]

As seen in figure 1.2, there are two distinct ranges of wavelengths (windows) that light is not absorbed in air in the infrared. These are named as 3-5 μm and 8-12 μm windows. To detect IR radiation at long distances, modern infrared detectors are specified to work at either one of these windows or both.

1.2 Detector Types

Photon detectors came into play in 20^{th} century in parallel with developments in quantum physics. First IR photon detector was invented by Case in 1917 [6]. Many types of detectors have since been developed some with much success and some even has been commercialized. Photodetectors can be classified as in two categories in terms of their operating principle; photoconductive detectors and photovoltaic detectors. Photoconductive types of detectors work by measuring the change in conductivity due to radiation falling onto detector. On the other hand, photovoltaic types of detectors work by measuring the change in electrical signal (current/voltage) due to radiation falling onto detector. The following is a short description of the most common photodetectors available today.

1.2.1 Mercury Cadmium Telluride (MCT)

MCT is a ternary semiconductor with a band gap depending on the mercury concentration and the temperature. $Hg_{(1-x)}Cd_{(x)}Te$ detectors are typically grown on CdTe substrates. Depending on Hg concentration, the largest lattice mismatch is 27%. Typical MCT detectors work as p-i-n diodes, energy band gap can cover 0-1.5 eV range depending on the mercury ratio. In other words, MCT detector can span the entire 1-20 μm window. MCT has a very high absorption coefficient over the 3-5 μm and 8-12 μm range that enables high quantum efficiency ($> 80\%$) [7]. MCT detectors have three major drawbacks. Because energy band gap depends sensitively on the alloy concentration, i) it requires precise control on the mercury composition ratio in the growth, ii) it suffers large leakage tunneling currents due to low electron effective mass, iii) large non-uniformities over large areas of the substrate during growth [8].

Despite the common drawbacks, current state-of-the-art technology of MCT detectors consist of large format 1024x1024 arrays on Ge substrates with 15 μm sized pixels in the 3-5 μm window. Ge substrate is preferred because the compatibility of in-situ and ex-situ surface preparations [9].

1.2.2 Quantum Well Infrared Photo Detectors (QWIPs)

QWIPs used for IR detection are the result of band-gap engineering technology in the GaAs/GaAlAs crystal system. Two materials with low (GaAs) and high (GaAlAs) band gaps are grown on top of each other resulting in a quantum well. With the control of thickness of the films, energy difference between ground state and the first excited state in the GaAs quantum well can be arranged in such a way that the difference equals the desired cut-off wavelength. The barrier (AlGaAs) between adjacent wells is thick enough to eliminate correlation of wave functions, hence tunneling at zero bias. Excited electrons are transferred to adjacent wells via tunneling which becomes possible due to band bending provided by the applying bias. Commonly used QWIP structure is GaAs/AlGaAs in order to use benefits of advanced GaAs technology.

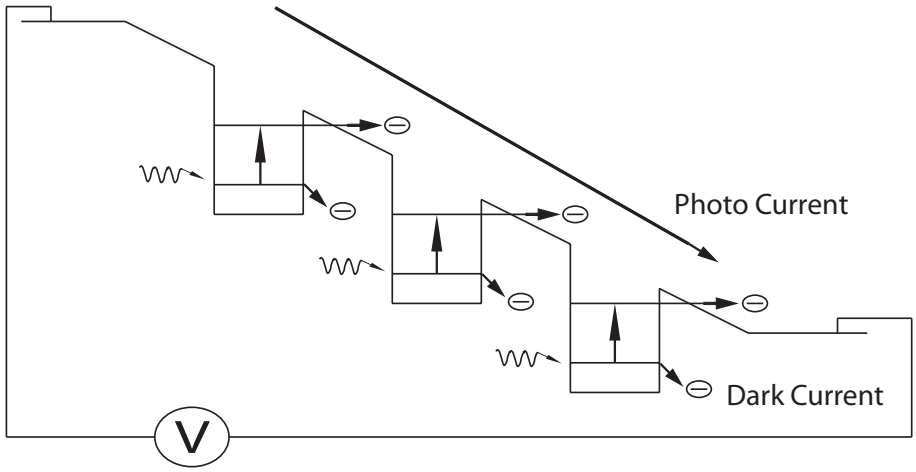

Figure 1.3: Schematic description of the operational principle of QWIPs

Besides the advantages like easy to growth on large areas and low cost through advanced technology, QWIPs have two major disadvantages: i) high dark current due to tunneling of thermal carriers ii) very low absorption at normal incidence illumination due to absorption selection rules which makes it necessary to use gratings if normal incident operation required. This reduces the quantum efficiency (20%) [10]. Current status of state-of-the-art QWIP detectors consist of 1024×1024 arrays and 25 μm sized pixels were introduced.[11]

1.2.3 Superlattice Photodetectors

Superlattice (SL) infrared photo detectors are the result of advanced band gap engineering technology based on the p-n junction. Like QWIPs, superlattice detectors consist of adjacent quantum wells. The difference between QWIPs and superlattice detectors is thickness of the wells. In superlattices, thickness of the well is on the order of 3-5 monolayer, thus wave functions of adjacent wells correlate which results in a mini-band. This type of structure is called superlattice.

Typical materials used in SL detectors are InAs and GaSb. InAs/GaSb SLs are called Type-2 superlattices because electrons in conduction band and holes in valence band are in different layers as shown in Fig. 1.4. This causes suppression of Auger recombination mechanism and results longer intrinsic life times than any other type of infrared detector material. Major disadvantages of SL detector are: Although dark current levels are very low, due to spatial separation of electrons and holes, optical absorption is low, too [12].

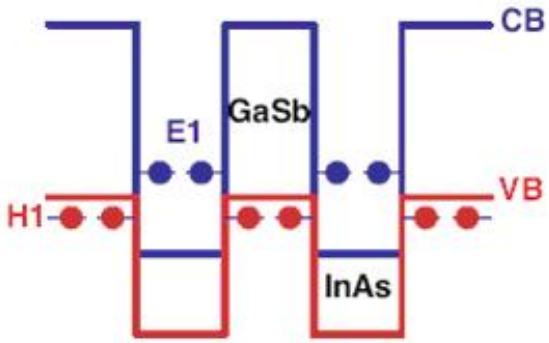

Figure 1.4: Band diagram of Type-2 superlattice

1.2.4 InSb Photo Detectors

InSb infrared photo detectors typically are, like MCT detectors, p-i-n diodes. A p-i-n detector consists of a p-n junction with an intrinsic layer inserted in between. The p-i-n diode is a two terminal device which requires ohmic contacts to both p and n sides of the diode, Fig. 1.5. This is done by coating both surfaces with appropriate metal and the underlying layers heavily doped to have low contact resistance. The p-i and i-n junctions have associated depletion layers (small in width on the heavily doped regions) with the intrinsic layer is depleted. The photocurrent is the sum of the charge generated per second in both diffusion regions p+ and n+ as well as the charge generated in the depletion layer, W, assuming that the thickness of the relevant layers is shorter than Lp , Ln and W. In the case of long diodes thermally generated current must also be taken into account [13].

$$I_{photo} = qA_gL_p + qA_gW + qA_gL_n \tag{1.4}$$

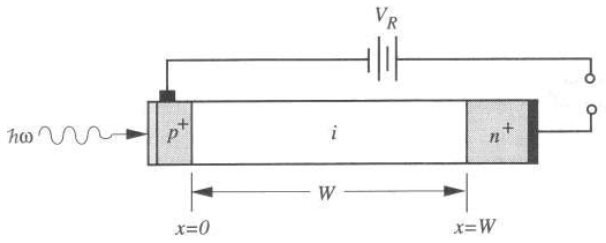

Figure 1.5: Structure of a p-i-n junction

For a diode to work as a photodetector it needs to be reverse biased in order to avoid the forward current. In the reverse bias, the band bending increases, Fig. 1.6. Photo generated electrons in the p region and holes in the n region diffuse into the depleted intrinsic region, where they drift to their respective terminals. Photogenerated carriers in the intrinsic layer are separated and drift due to the applied electric field.

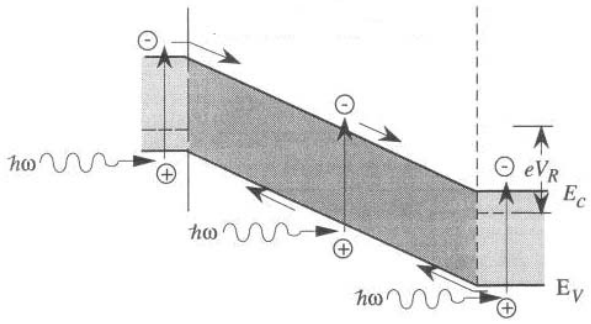

Figure 1.6: Operation scheme of a p-i-n photodiode

InSb has a band gap of 0.225 eV at 77 K and 0.175 eV at 300 K [14] and [15]. This corresponds to a cutoff wavelength of 7 μm at 300 K and 5.5 μm at 77 K [16]. Although band gap at 300 K shows the cutoff wavelength as 7 μm, InSb detectors require cooling. At room temperature, intrinsic carrier concentration of pure InSb is $2 \times 10^{16}\ cm^{-3}$, which leads to high dark currents [17]. Doping of material to create n and p-type regions raises this concentration, thus at room temperature, InSb detectors do not behave like diodes, but as resistors that are short-circuited with huge dark currents. When cooled down to 77 K, carrier

concentration drops to 5×10^{10} cm^{-3} [18]. This limits the working temperature of InSb detectors. Temperature dependence of intrinsic carrier concentration is shown in Eq. 1.5

Carrier Concentration →

$$n = n_0 e^{\frac{-E_g}{kT}} \tag{1.5}$$

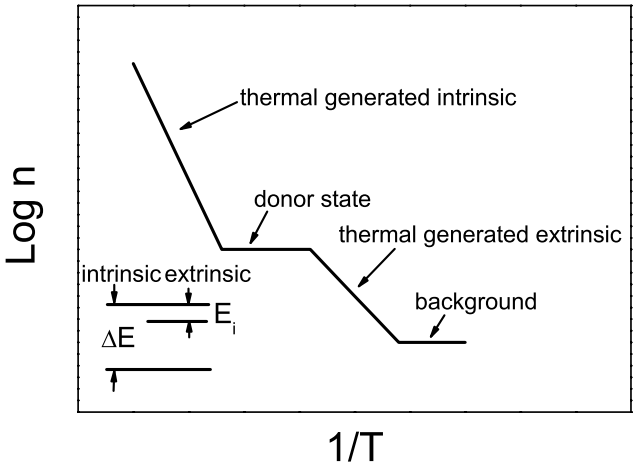

Figure 1.7: Temperature dependence of carrier concentration in doped semiconductors

InSb detectors simply work in 3-5 μm window. High optical absorption of shorter wavelengths makes detection of wavelengths shorter than 3 μm difficult. Similarly, the insufficient energy of longer wavelengths to generate electron-hole pairs make the detection of those wavelengths impossible. Fig.1.8 shows the absorption coefficient of pure InSb.

Quantum efficiency of InSb detectors is independent of temperature between 60 K and 80 K and is typically around 60% [19]. Another advantage of InSb is the possibility of growing it on large substrates, making it possible to fabricate 2048×2048 arrays with 20×20 μm^2 sized pixels. Major drawback of InSb detectors is non-uniformity of dark current level from cool down to cool down because

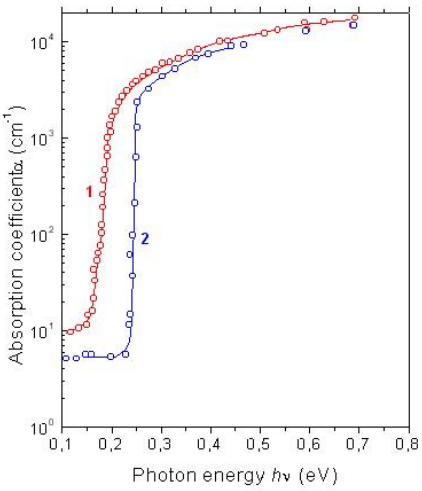

Figure 1.8: Absorption coefficient of InSb, 1) 300 K, 2) 5 K [1] and [2]

of water-ice film depositing on the detector, which requires making calibrations periodically [20] and [21].

The basic mechanisms that contribute the dark current are: diffusion, surface diffusion, generation-recombination, tunneling, and the surface leakage. Bulk diffusion current is caused by minority carriers (electrons) in the p region diffuse to the n region becoming majority carriers, thus contributing to dark current, vice versa. Generation-recombination current is the result of generation of electron-hole pairs in the depletion region which are not caused by radiation but due to thermal energy of carriers. Tunneling current is because of the tunneling effect in the junction, it is directly proportional with the applied bias because higher bias values bends band more, and this increases the tunneling probability. Shunt current is caused by the ohmic leakages along the edges and the dislocations in the crystal [22] and [23].

$$I_{dark} = I_{diffusion} + I_{g-r\ current} + I_{tunneling} + I_{shunt} + I_{surface\ diffusion}$$

$$\frac{1}{R} = \frac{1}{R_{diffusion}} + \frac{1}{R_{g-r\ current}} + \frac{1}{R_{tunneling}} + \frac{1}{R_{shunt}} + \frac{1}{R_{surface\ diffusion}}$$

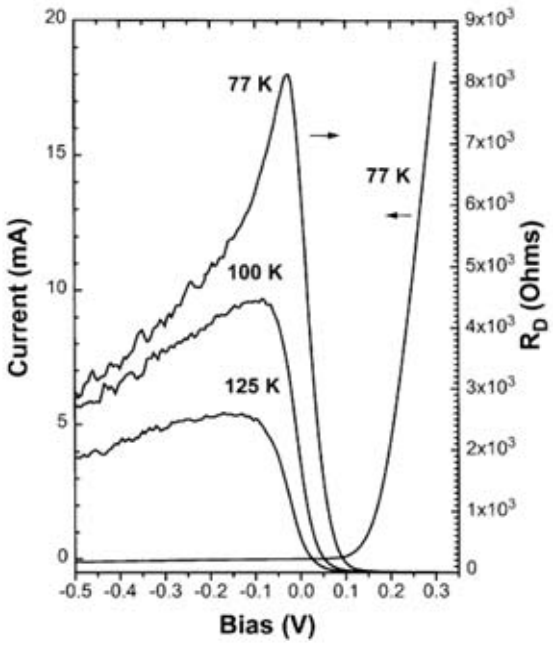

Figure 1.9: Typical dark I-V curve and R vs. Bias voltage [3]

$$
\begin{aligned}
I_{diffusion} &= A\,T^3\,e^{\frac{-E_g}{kT}}\,\left[e^{\frac{qV}{kT}}-1\right] \\
I_{g-r\ current} &= B\,T^{3/2}\,e^{\frac{-E_g}{2kT}}\,(V_b-V)^{(1/2)}\,\left[e^{\frac{qV}{2kT}}-1\right] \\
I_{tunneling} &= C\,\left[(V_b-V)^{1/2}\frac{V}{E_g^{1/2}}\right]\,e^{-F\left[\frac{E_g^{3/2}}{(V_b-V)^{1/2}}\right]} \\
I_{shunt} &= D\,V\,T^{3/2}\,e^{\frac{-E_g}{2kT}} \\
I_{surface\ diffusion} &= G\,T^{3/2}\,e^{\frac{-E_g}{2kT}}\,\left[e^{\frac{qV}{kT}}-\frac{qV}{kT}-1\right]^{1/2}
\end{aligned}
$$

where V_b is built-in potential when junction is formed, V is the applied bias, T is temperature, k is Boltzmann constant, q is the unit charge and kT/q is the thermal voltage and A, B, C, D, F and G are the fitting parameters. Besikci *et al.*, tried to fit above equations to the experimental data [3]. Below figure

shows the experimental data and the fitted five equations. They adjusted the fitting parameters according to experimental data and then plotted the five effects separately.

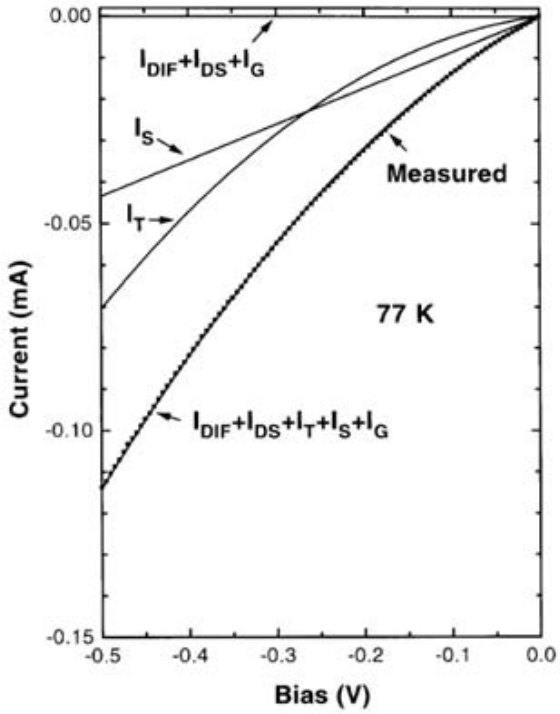

Figure 1.10: Dark current components at 77 K [3]

Fig.1.10 shows that at 77 K, diffusion current in the bulk and on the surface, and the generation-recombination current is negligible for all bias values. The dominant leakage mechanism is shunt (surface leakage) current and tunneling. Near zero bias, the dominant mechanism is the shunt current since the tunneling probability is low at low biases. As bias increases, tunneling becomes dominant. This can be explained as surface leakage is a parallel resistance to the system, thus shunt current is increasing linearly but tunneling current increases exponentially. This can also be seen in Fig.1.9, tunneling current is independent of temperature but shunt current is highly dependent on temperature. Resistance of the detector is independent of temperature for large bias values, which suggests, that tunneling is the dominant leakage mechanism in this case [3].

1.3 Figures of Merits

Figure of merit is a quantity used to characterize the performance of a system that enables us to compare different systems. These figures are important for the comparison of different detectors. They are basically, the specifications of the infrared photo detectors.

1.3.1 Quantum Efficiency

Quantum efficiency is the number of carriers measured at the output of detector per number of incident photons per unit time. It shows the ability of the detector to convert incident photon flux into electrical signal and is given as:

$$\eta = \frac{I_p}{qA\varphi} \tag{1.6}$$

where I_p is the output photocurrent, A is the active detector area, q is electron charge, and φ is the incident optical flux. Quantum efficiency is a measure of the number of generated electron-hole pairs created by photons, so by definition, η is less than 1.

1.3.2 Responsivity

Using quantum efficiency, we can also define responsivity. Responsivity is the output electrical signal divided by input optical signal:

$$R = \frac{\text{Output Signal}}{\text{Input Signal}} = \frac{\eta q}{h\nu} \tag{1.7}$$

Typical unit of responsivity is A/W or V/W where hν is energy of incident photons. If wavelength of the incident photons is integrated to the responsivity,

it is called spectral responsivity. Fig. 1.11 shows a typical spectral responsivity curve.

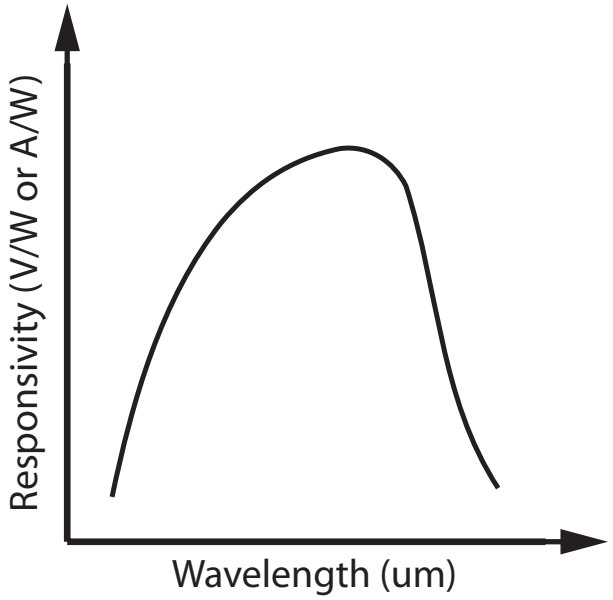

Figure 1.11: Spectral responsivity

1.3.3 Background Limited Detection

Background limited operation indicates the largest temperature at which the photo current to dark current ratio becomes 1, i.e, $I_{(photo)} = I_{(dark)}$. When the detector is operated at this temperature, the detector is said to operate as a background limited infrared photodetector (BLIP).

Chapter 2

Experiment

2.1 Design Considerations

For photovoltaic operation, a p-n junction is needed to transport the generated carriers to the contacts. To increase the absorbed radiation, an intrinsic layer is inserted between the p and n layers. There is a trade-off at this step; if intrinsic layer is thick, large amounts of radiation is absorbed, on the other hand, photo generated carriers may recombine before reaching the contacts which causes a decrease in the photocurrent. The carrier diffusion length in InSb has been measured to range betweeen 28-50 μm [24] and [25]. Since a detector with an intrinsic layer of this thickness is very expensive to grow, we had to choose a much thinner layer to fabricate, test and compare various passivation techniques. On the other hand, if the intrinsic layer is very thin, efficiency is reduced because of low absorption. We optimized the intrinsic layer thickness that both enables high radiation absorbance and thin enough for generated carriers reach to the contacts in their short lifetimes as microseconds for holes and nanoseconds for electrons [26]. The epitaxial structure was grown on semi-insulating GaAs substrate by molecular beam epitaxy. GaAs substrate is used for making use of developed GaAs technology. A 1.5 μm AlSb layer was grown before the growth of the InSb layers to reduce lattice mismatch from 14.7% to 5.5% as shown in Fig.2.2

to increase the quality of InSb epitaxial layers [27]. AlSb can also serve as an etch stop layer for future backside illumination applications. A 0.5 μm InSb unintentionally doped buffer layer was grown before the growth of doped InSb layers. This buffer layer eases the transition from AlSb to n+ InSb. The photo detector consists of a 1-μm-thick n+ InSb layer at the bottom, 2.5-μm-thick intrinsic InSb layer, and a 0.5-μm-thick p+ InSb layer at the top. The intrinsic layer was unintentionally doped to less than $1 \times 10^{16}\ cm^{-3}$, while the highly doped layers were doped to $1 \times 10^{18}\ cm^{-3}$. p+ and n+ layers were doped with beryllium and tellurium, respectively. The growth was done at IQE Inc. (Bethlehem, PA)

Figure 2.1: Scheme of the structure

2.2 Fabrication

In this section, process design and fabrication process of InSb infrared detectors will be explained. First step is designing a mask. For characterization of the InSb detectors, we have mesas ranging from 100 to 600 microns since we are not considering focal plane arrays in the first place which require smaller pixels. A photo detector is a two terminal device requiring ohmic contacts both at n+ and p+ regions. The contact to p+ surface can easily be done but one has to reach

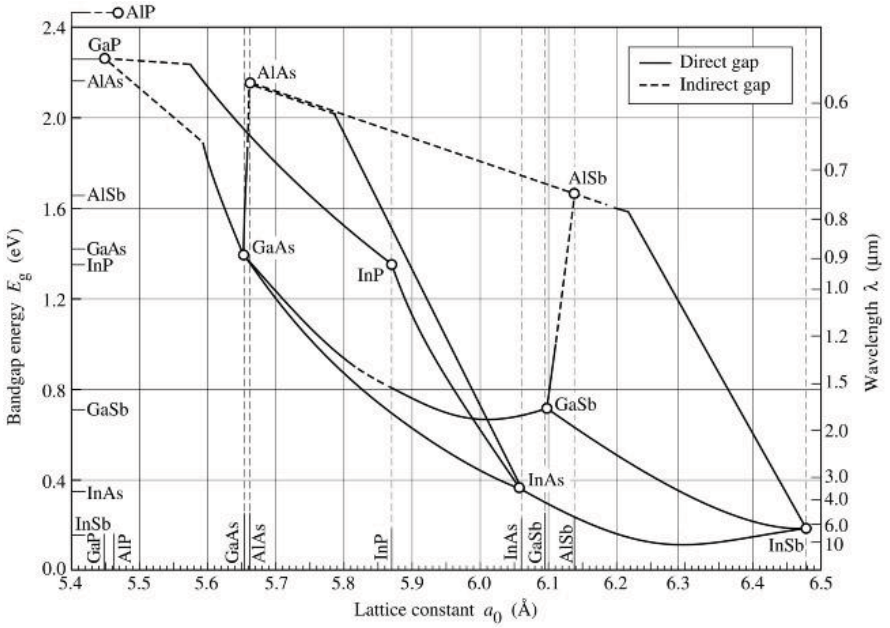

Figure 2.2: Lattice constant vs. band gap energy [http://www.ee.ucla.edu/∼wu/ee174]

down to n+ region, thus mesas have to be defined first. For the p layer contacts, our priority concern is getting as much radiation as possible and good electrical conduction. For that purpose, 50 micron thick squares centered on the top of mesas are designed. For the n layer contacts, we designed them in such a way that whole n layer between the mesas was coated with ohmic contact. Passivation mask is designed so that passivation starts from topside of the mesas down to the n layer.

Fabrication process starts by defining the mesas and etching sample down to halfway of the n+ layer. First, sample is cleaned via three solvent cleaning processes. Then, photo resist is spun on sample. UV lithography is done using MJB3 Karl Suss mask aligner. Our mask has five different mesa sizes, 100, 200, 400, 500, and 600 μm wide squares. Mask scheme can be seen in Fig.2.3. Process steps are schematized in Fig.2.4. Fabrication step details are in Appendix A.

Mask is designed as in Fig.2.3 using L-Edit software. As seen, mask consists of 4 symmetric patterns; every pattern has 10 of 600 μm wide mesas, 10 of 500 μm

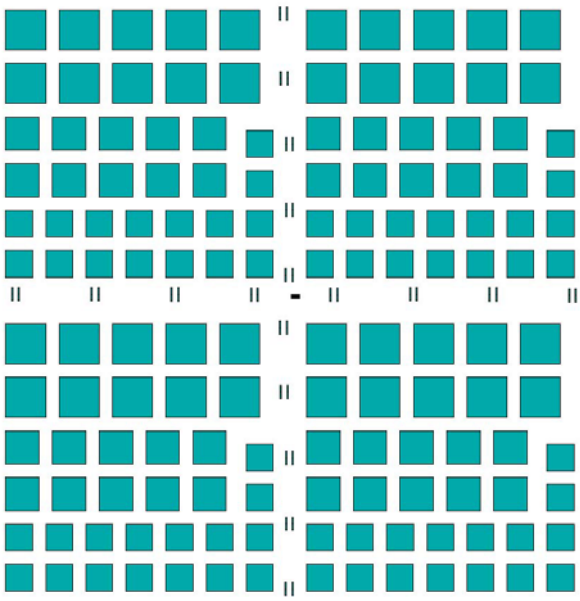

Figure 2.3: Mask scheme for 400, 500 and 600 μm mesas

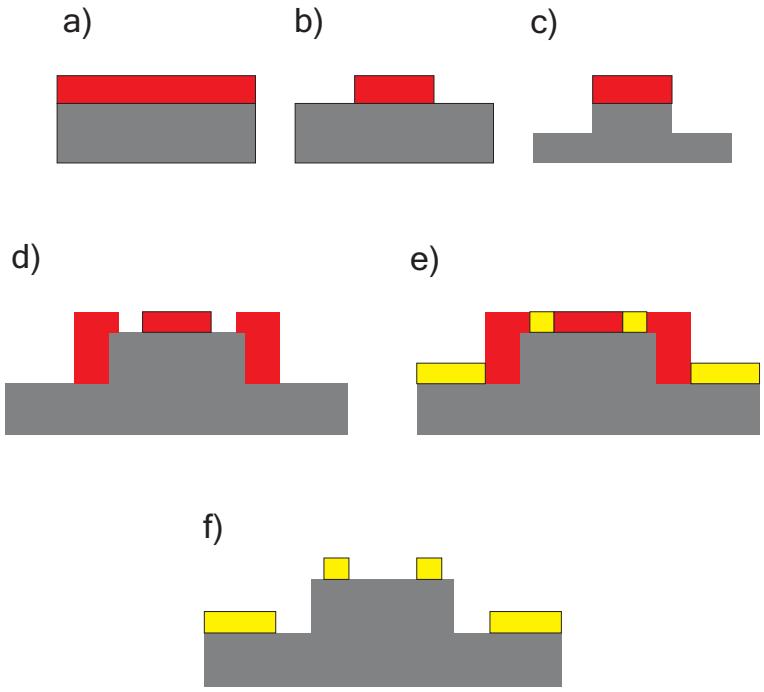

Figure 2.4: Schematic of fabrication steps a) photo resist is spun on wafer, b) lithography is done, c) wet etching done, d) metallization mask, e) metal deposited, f) after liftoff process.

wide mesas and 16 of 400 μm wide mesas. Thus, we can generate a total of 144 single pixel detectors in a 1x1 cm^2 sample area. As seen in Fig.2.12, samples are cleaved into 4 pieces and each can be used to try different passivation approaches. For 100 μm and 200 μm mesas mask scheme and fabrication steps are different because of the difficulty of bonding on smaller areas. They will be mentioned on Chapter 4.

Mesa etching is done with a citric acid: hydrogen peroxide (50:1) solution and the etching time was optimized [28]. Etch depth vs. time graph is given in Fig.2.5, total etch time is approximately 3-3.5 hours. A slow rate is chosen to avoid rough surfaces at the end of the wet etch which may increase leakage currents. Sample is post-baked at 120 ^oC for 10 minutes to harden the photo resist for etching process. Etch profile is investigated in Scanning Electron Microscope (SEM) and picture of the etch profile is given in Fig.2.6 and Fig.2.7. As we need to get contacts from n+ layer and p+ layer, after etching the sample halfway into of the n+ layer, another lithography step is needed for metallization. Since infrared radiation is incident on p layer, p+ layer metallization pattern is designed to be at the edges of the mesas for the purpose of maximum infrared radiation absorption.

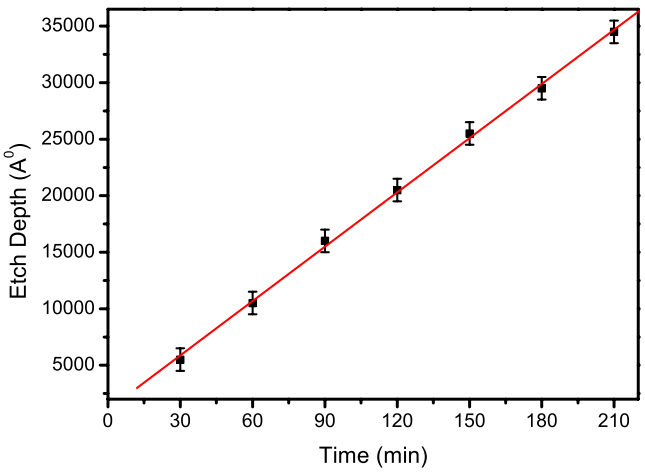

Figure 2.5: Etch depth vs. time (The line is drawn to guide the eye)

Metallization is done in the box coater using thermal evaporation. 500/3000 Angstroms Ti/Au is coated to obtain ohmic contacts [29]. Lift-off process is

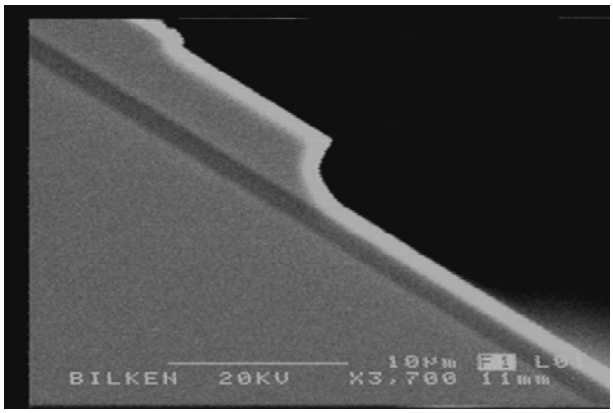

Figure 2.6: SEM picture of etch profile

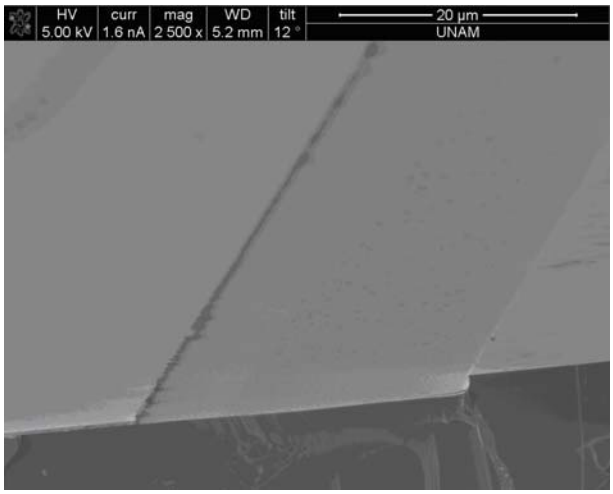

Figure 2.7: SEM picture of etch profile

done in warm acetone medium. Contacts were found to be ohmic at 77 K even when no annealing was applied. Measurement was done via transmission line method (TLM) as shown in Fig. 2.8. Resistance between between metal and semiconductor is on the order of 2 Ω between [-1,1] mA and [-100, 100] mV range as shown in figure 2.9. We used TLM to measure the contact resistance between metal and semiconductor surface. 200x200 μm^2 metal coated squares were fabricated with distance between adjacent squares ranging from 5 to 100 μm. Resistances are calculated by measuring I-V curves of each adjacent pair. Interpolating the graph of total resistance versus length gives us the twice of the contact resistance between metal and semiconductor, as shown in Eg. 2.1 total resistance equals to twice of contact resistance.

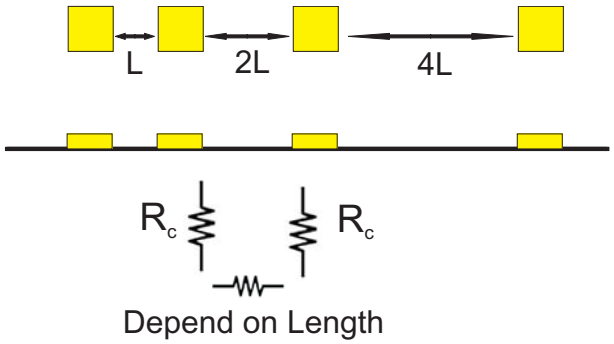

Figure 2.8: Transmission Line method

$$R = 2R_c + (\frac{\rho}{A})L \tag{2.1}$$

After all three processes are done; some pairs of samples were treated in O_2 plasma to remove organic residues. O_2 plasma is done in the RIE system, O_2 gas flow at 20 sccm, with pressure 20 μbar, RF power was 100 watt, and the process time was 2 min. On the other hand, other samples were cleaned via three solvent cleaning methods to remove organic residues such as photo resist. Thus at the end, we have two different non-passivated types of samples to see the effect of the O_2 plasma. Microscope images of the sample at various process steps are shown in Fig. 2.10. Top view of the detector, Fig. 2.11, shows the quality of the process.

After fabrication process is done, samples are bonded onto electronic packages.

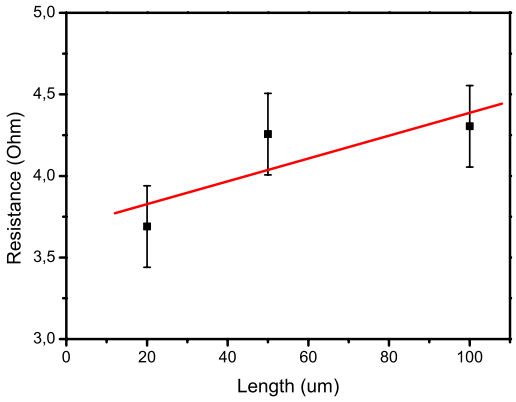

Figure 2.9: Total resistance vs. length as obtained from TLM

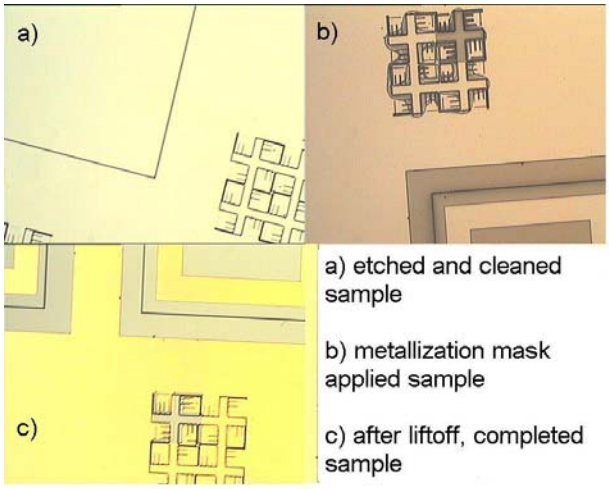

Figure 2.10: Microscope images of the sample at various process steps

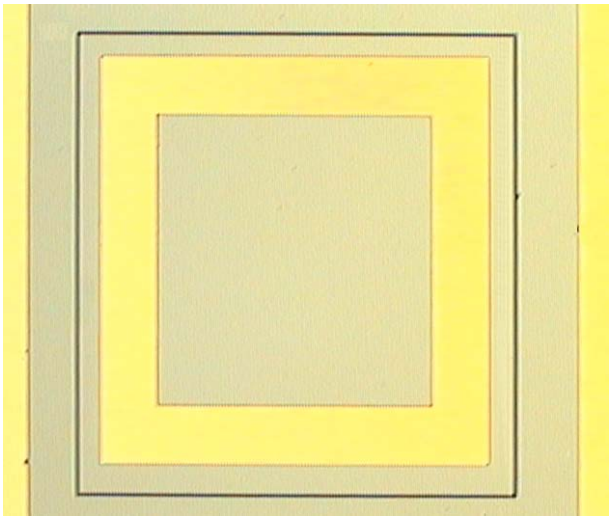

Figure 2.11: Top view of the detector

First, samples are attached to the package via thermal compound used in computers to provide thermal contact. Bonding process is done at WestBond bonding station. 12 μm diameter gold wire and (f2525m) wedge tip are used for bonding. A picture of ready-to-measure sample is shown in Fig.2.12.

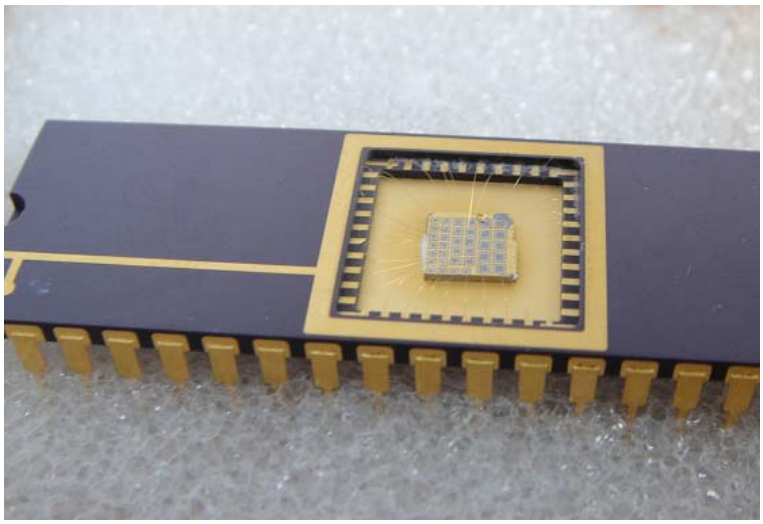

Figure 2.12: Ready to measure sample

Chapter 3

Measurement and Results

This section provides information about characterization of detectors. At room temperature, there are so many thermally generated carriers that detector shows no diode characteristics. First of all, we need to cool down the detector to reduce thermal carriers. We used liquid nitrogen for cooling. All measurements were done at 77 K. Current-voltage characteristics of the detectors were measured using a modular source/monitor unit, HP 4142B. Max current was limited to 1 mA to prevent overheating of the devices. Spectral response measurements are done via a modified FTIR system.

3.1 Dark Current Measurements

Dark current of a photo detector is a function of bias voltage only when detector generates in the absence of IR light [30]. To build up such environment, sample is lowered into liquid nitrogen facing downwards and also is covered by aluminum shields. Therefore, no outside light can pass to the detector as seen in Fig.3.1.

I-V characteristics were measured when the sample reached thermal equilibrium. Since different sized mesas showed different dark currents, we assume ohmic leakage along the edges depends on the sample size. Further, two types of samples

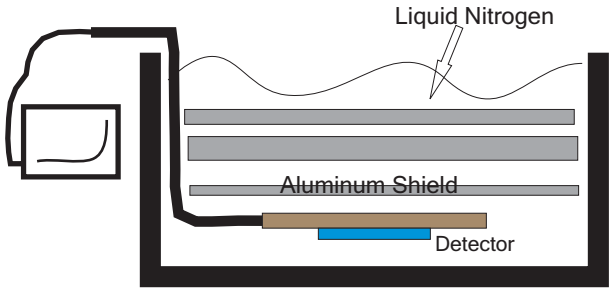

Figure 3.1: Dark current measurement setup

mentioned in the previous chapter (O_2 plasma treated and three solvent cleaned samples) were expected to differ in their dark current. We take -100 mV as reference bias for current and current density vs. mesa area graphs. Fig.3.2 and 3.3 show the I-V curves for different mesa sizes and treatments. These are I-V curves are for non-passivated samples. Surface leakage is proportional to the sidewall area, however since all etch depths are equal it is sufficient to use mesa sizes to compare. Fig.3.2 and 3.3 inset show that the dark current changes linearly with mesa size. The reason for the linear dependence of the dark current with the mesa size is related to the sidewall areas which changes linearly with mesa sizes [31]. When we plot current density vs. mesa area, we note that current density remains the same for all mesa sizes. As seen from Fig.3.2 and Fig.3.3, O_2 plasma treated samples show a decrease of almost 5 times in dark current. At least 10 mesas were measured for each of different sized mesas and the average is reported. Dark current at -100 mV bias for samples that are only three solvent cleaned with an area of 400x400 μm^2 is 140.00 μA, but the that are O_2 plasma treated show an average dark current of 20,65 μA. For 500x500 and 600x600 μm^2 area samples, corresponding values are 224.43, 35.65, 256.8, 42.44 μA, respectively. Standard deviations of the current are $\pm$ 10.00 μA for three solvent cleaned samples and $\pm$ 5.00 μA for O_2 plasma treated samples. By looking at these error values, we can say that the results for the O_2 plasma treated samples are more consistent than the others.

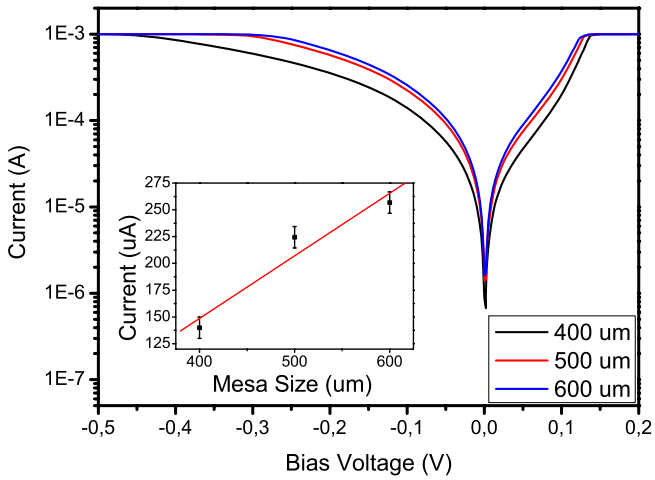

Figure 3.2: Dark I-V curves of the three solvent cleaned samples, Inset I_{dark} at -100mV vs. mesa size (the line is drawn to guide the eye)

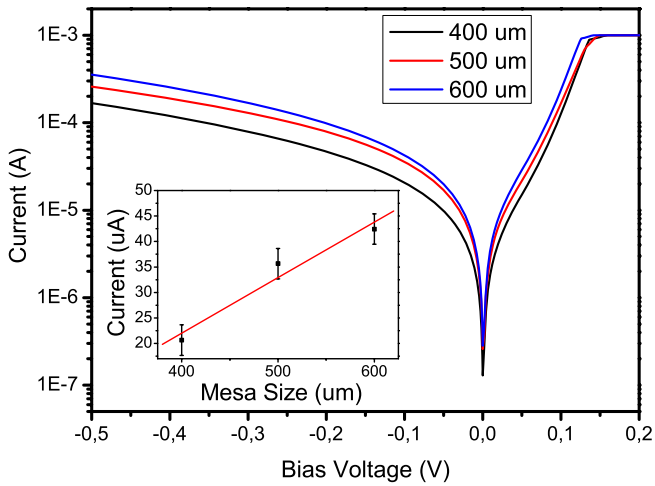

Figure 3.3: Dark I-V curves of the O_2 plasma treated samples, Inset I_{dark} t -100mV vs. mesa size (the line is drawn to guide the eye)

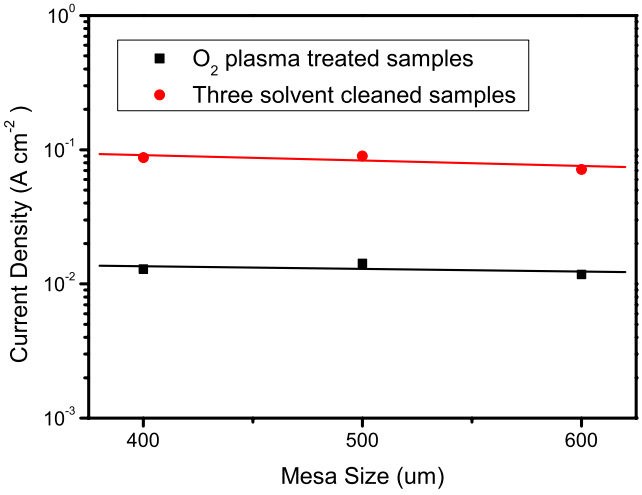

Figure 3.4: Dark current density vs. mesa size graph at -100 mV bias (the line is drawn to guide the eye)

3.2 Photo Current Measurements

Photocurrent is the current occurs when detector is exposed to light. Detector is still left in liquid nitrogen environment but it now faces upwards and the field of view is nearly 180 degrees ($f\# \sim 0$) as shown in Fig. 3.5. Photocurrent is measured in lab environment under ambient illumination. Photocurrent is the total current read at this setup configuration minus the dark current. When the photocurrent is equal to the dark current, background limited operation condition is satisfied. In our samples, O_2 plasma treated samples are already below the BLIP limit. This means, these detectors can work at higher temperatures. However, detectors that have received the standard cleaning treatment are above the BLIP limit at liquid nitrogen temperature, thus, they need to be cooled down more to achieve BLIP condition.

Fig. 3.6 shows photo current and dark current vs. bias voltage graph for 400x400 μm^2 area O_2 plasma treated samples. Dark current and photo current measurements were done at the same time, so again at least 10 mesas of different sized mesas were measured. Average photo current of non-passivated samples at -100

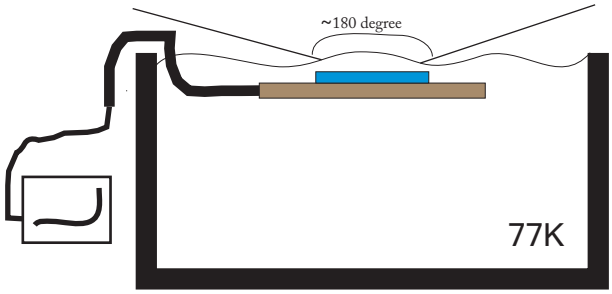

Figure 3.5: Photo current measurement setup

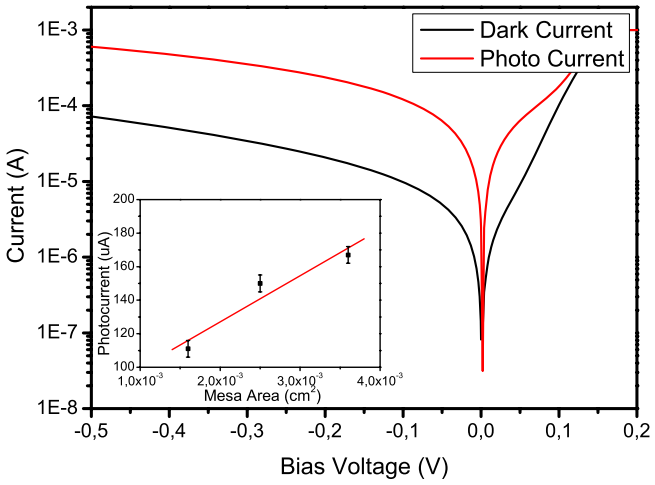

Figure 3.6: O_2 plasma treated 400x400 μm sized mesas dark and photo currents, inset photo current vs. mesa area at a bias of -100 mV (the line is drawn to guide the eye)

mV bias are 111.0, 150.0, 167.0 μA for 400x400, 500x500, 600x600 μm^2 area samples, respectively.

3.3 Spectral Response Measurements

Spectral response of detectors is measured via Fourier Transform Infrared Spectroscope (FTIR) in a custom setup. First, sample is cooled down to 77 K in a closed loop liquid helium cryostat and an infrared transparent window is used for the detector facing towards to FTIR output. FTIR directly measures the spectral response of the detector with respect to background signal. Background is taken with our detector while detector sees none from FTIR source.

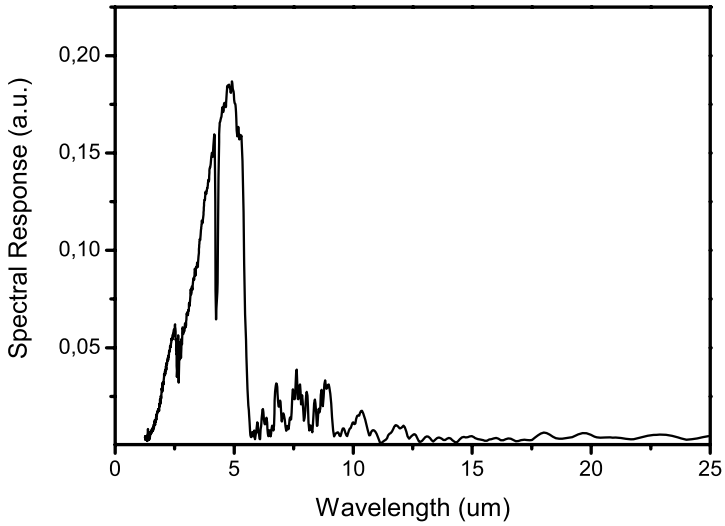

Figure 3.7: Raw spectral response data

In figure 3.7, raw FTIR data of spectral response is presented. As it is seen in the figure 3.7, signal is maximum for 3-5.5 μm window, signal in the 6-10 μm region is due to improper substraction of the backgorund. Due to the range of interest, rest of the spectral response graphs are plotted between 3-5.5 μm.

Fig.3.8 shows the spectral response of our detectors in arbitrary units. Again, at

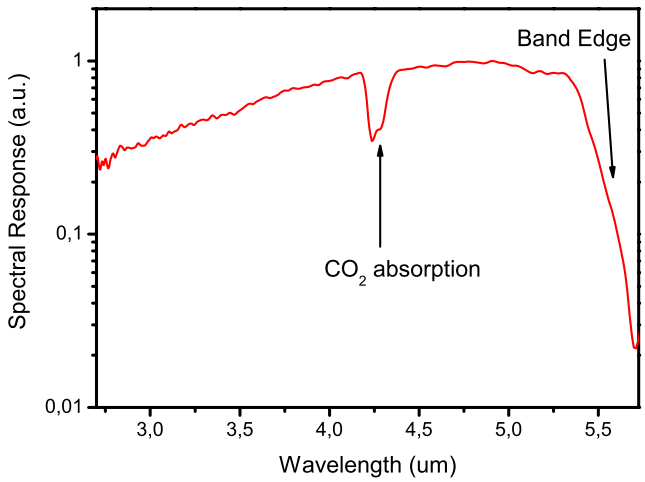

Figure 3.8: Responsivity graph of the sample

least 10 mesas of different sized mesas were measured. For different sized mesas, spectral response curve shape is same as expected. Relative signal intensity is different for different sized mesas as seen in Fig.3.9 because more light on detector means more current.

Dip at 4.3 μm corresponds to absorption CO_2. CO_2 absorption is well-known, so other figures have been corrected for CO_2 absorption. Fig.3.10 shows the change in the spectral response with respect to applied bias. Response increases with increasing bias, since the collection efficiency of the generated carriers increase with the increasing bias. It saturates because once all available generated carriers are collected, we can no longer increase the collection efficiency. In the positive bias region, dark current is so large that photo current to dark current ratio is very low, thus spectral response is negligible.

As InSb has a band gap at 5.5 μm (0.225 eV) at 77 K, light with longer wavelengths does not have enough energy to generate electron-hole pairs. Wavelength corresponds to band gap energy of the crystal is defined as cut-off wavelength. Wavelengths below 3 μm should be detected in principle (in the light of the above argument) but absorption coefficient of InSb increases abruptly for wavelengths shorter than 3 μm. Thus, shorter wavelengths cannot be detected since they are

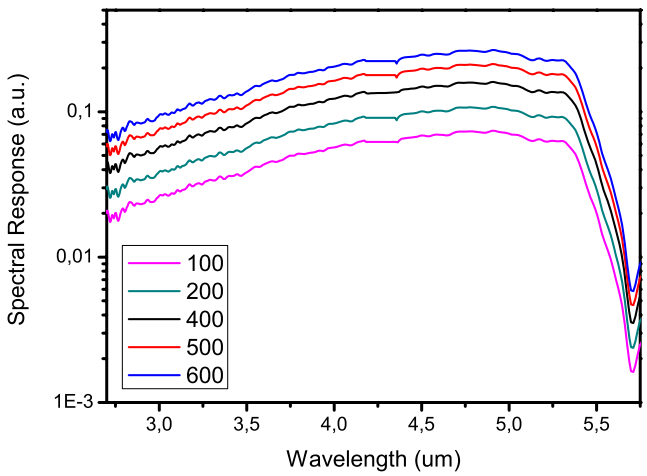

Figure 3.9: Spectral Response at zero bias vs. mesa size

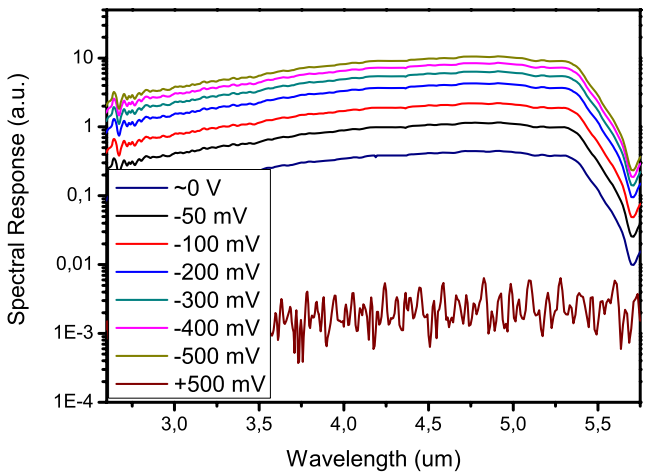

Figure 3.10: Spectral response vs. bias voltage

absorbed very near the surface.

3.4 Calculations

3.4.1 Resistance

To see how flat the dark current in the negative bias region is, resistance of the detector has to be known. To be able to compare our detector with other detectors, area dependence of resistance needs to be eliminated. Thus, $R \times A$ value is used commonly; here A is the detector area. Our detectors have R_0 values up to 15 $K\Omega$, average being 5 $K\Omega$ for 400 μm detectors and $R_0 \times A$ values up to 20 Ωcm^2 and average being 10 Ωcm^2 almost for all detector sizes as shown in Fig. 3.12. Resistance is plotted with respect to bias in Fig. 3.11 for different mesa sizes. Resistance of the detector is decreasing with the increasing reverse bias because of increasing dark current. These values are bettter than those in [29] by a factor of five.

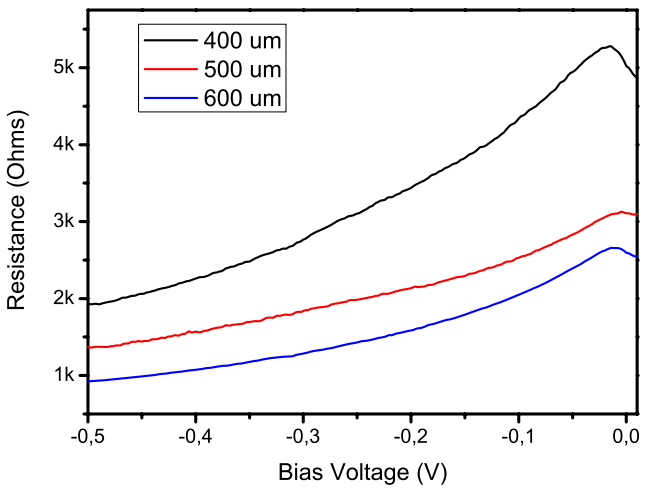

Figure 3.11: Resistance vs. bias voltage graph of O_2 plasma treated samples

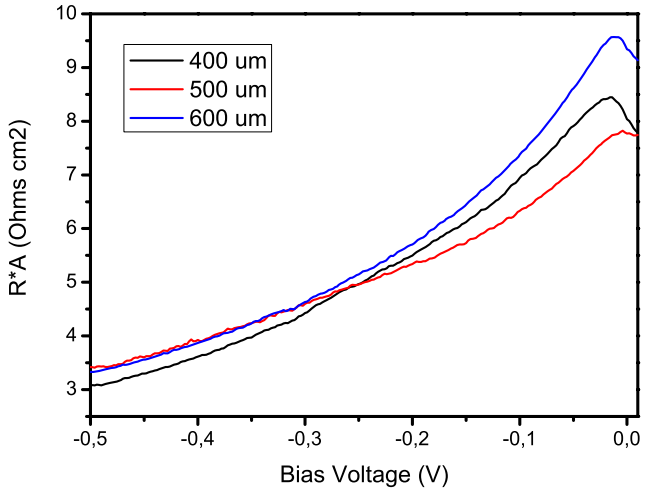

Figure 3.12: R×A vs. bias voltage graph of O_2 plasma treated samples

3.4.2 Responsivity

As defined in section 1.3.2, responsivity is current (A) or voltage (V) signal output from the detector over the optical signal input (W). In the absence of a true blackbody source, we used an approximate method to calculate responsivity of our detectors. Error in this method is within a few percent, and results are underestimated. This method is widely used to determine the responsivity without using a blackbody [32] and [33]. In Section 3.2, we have measured the signal output as photocurrent. This measurement is done with the detector facing the lab environment under ambient illumination while the detector is at 77 K. We, therefore, assume that the optical power incident onto the detector is that of a blackbody at 300 K. Output current (photocurrent) has been reported in previous section. Output current divided by the input optical power onto detector is the responsivity, provided the detector response is flat. We, then calculate the ratio of the areas under the normalized responsivity curve of our detector and that of a detector with a flat response. Multiplying the responsivity value found earlier with this ratio results in the peak responsivity value at a particular wavelength as well as the actual responsivity as a function of wavelength. As mentioned earlier, responsivity is not the only quantity to compare photo detectors. A detector can

have a high responsivity values but can also have very high dark current. Fig.3.13 shows responsivity graph for our detectors. We have an peak value of 90 A/W at 4.91 μm at -100 mV bias for 400 μm detectors. The maximum obtained value is 170 A/W for one of the 400 μm sized detectors. For InSb photodetectors with different areas, average responsitities are 75 A/W and 60 A/W for detectors with areas of 500x500 μm^2 and 600x600 μm^2, respectively. In contrast with expectations, we note that there is a trend of increasing responsivity with decreasing mesa area. This indicates a better collection efficiency of photo generated current for smaller mesa areas which is reasonable in the light of the fact that this is a strained crystal which would have a large number of defects.

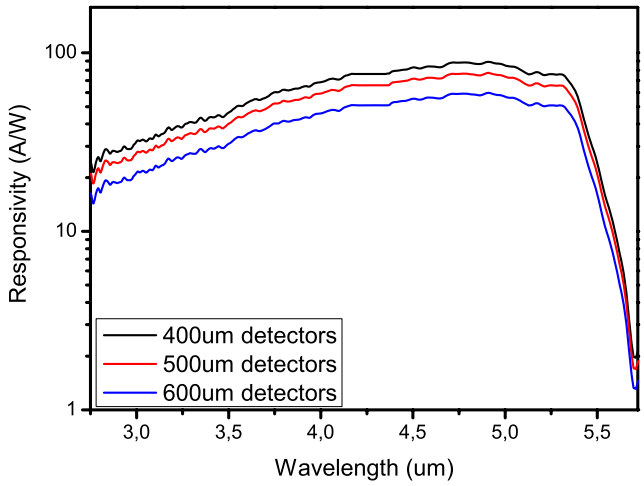

Figure 3.13: Responsivity of InSb detectors

Chapter 4

Passivation Techniques

4.1 Introduction

Up to this point, we fabricated InSb p-i-n junctions and measured the output signal both in radiation environment and in the absence of it, and also the spectral response of the detectors. Next step is to improve the photo current to dark current ratio. Theoretically, dark current of an ideal p-i-n junction should be zero. But for reasons explained in Chapter 1, however this is not true in reality. The most dominant mechanisms for the dark current are tunneling current and the ohmic surface leakage as seen in Fig.1.10. Once the crystal structure is defined, there is not left much to reduce the effect of tunneling. The best thing to do is try to find how to reduce ohmic leakage and Maniv suggests that dark currents are mostly due to surface leakage caused by dangling bonds [31]. And these leakages can be minimized by passivating the edges via an insulating material [34] and [35]. Dangling bonds (or surface states) occur in the process of mesa etching. Elimination of dangling bonds is done by binding these bonds via an insulating material. In the literature, insulator materials mostly used are SiO_2, SiN_x and Sulphure solutions [36] and [37] and[38] have also been used with some success. We first tried these three materials as a passivating material to make a comparison of our detectors with the results in the literature. Passivation is done

by deposition of thin films (SiO_2 and SiN_x) to the edges of the detector. However, sulphure solutions are in aqua form hence the method of applying sulphure solutions is different than the other two methods.

4.2 Passivation Process

For SiN_x and SiO_2 passivation, we used PECVD to grow films. Typically, thin films of dielectrics 300 nm thick are grown. After the film is grown over all of the surface area, a lithography step is needed to get rid of the film on metal contacts to get good electrical contact. After lithography, sample is baked at 120 ^oC to harden the photo resist. The samples are then immersed into a buffered HF solution (1:10) for 60 sec, and rinsed in DI water. They are then blow dried with nitrogen and soaked in acetone to remove the photo resist. Fabrication steps are illustrated in Fig.4.1. The recipe used in the PECVD step to grow the insulating SiO_2 layer is 180 sccm SiH_4, 45 sccm N_2O and the pressure is 1 Torr for SiO_2. For the deposition of SiN_x, 180 sccm SiH_4, 45 sccm NH_3, and 1 Torr pressure is used. All films were grown at a substrate temperature of 250 ^oC. Sulphure solution passivation is done by soaking the fabricated samples into buffered $(NH_4)_2S : H_20$ (1:1) solution for 30 minutes under the fume-hood. Samples are then blow dried with nitrogen.

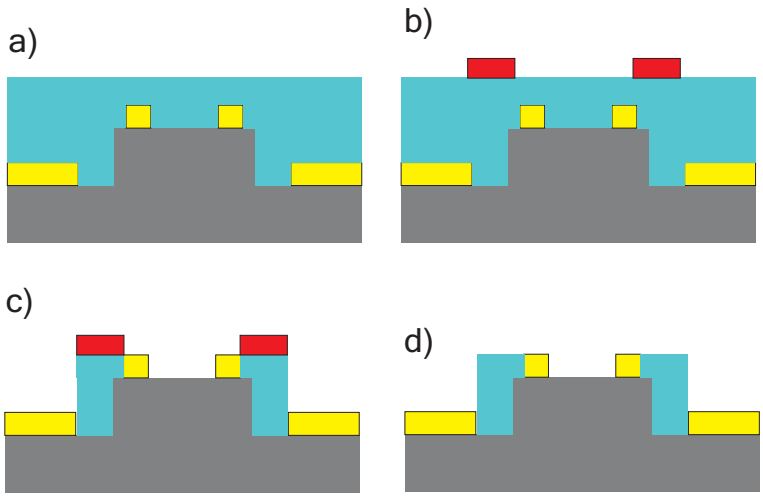

Figure 4.1: Passivation scheme

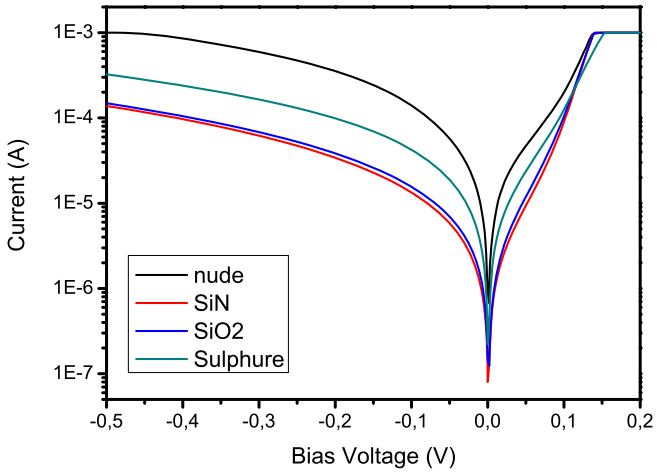

Figure 4.2: Dark I-V curve of samples with 400x400 μm^2 mesas passivated after three solvent cleaning

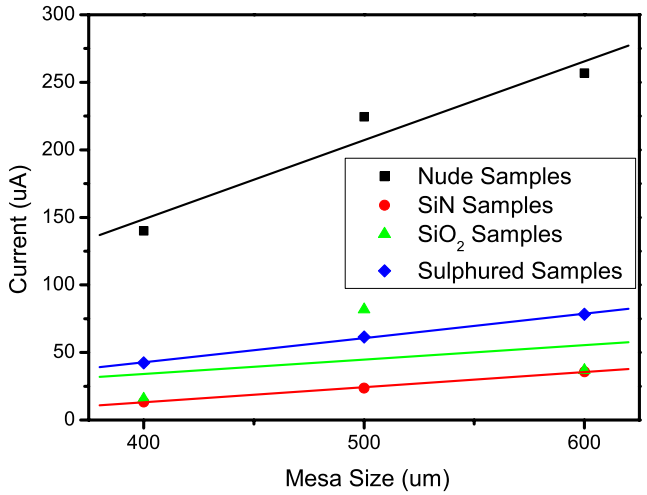

Figure 4.3: Dark current vs. mesa size passivated samples with prior three solvent cleaning at a bias of -100 mV (the lines are drawn to guide the eye)

Passivation applied to samples that are three solvent cleaned results in a large decrease in the dark current. The current before passivation for 400x400 μm^2 detectors is typically 140.00 μA at -100 mV bias, with SiN_x passivation 400x400 μm^2 detectors show 13.36 μA dark current which means that the passivation reduced the dark current 10 times. Dark current value is 15.55 μA and 42.33 μA for SiO_2 and sulphured solutions, respectively as in Fig. 4.2 and 4.3.

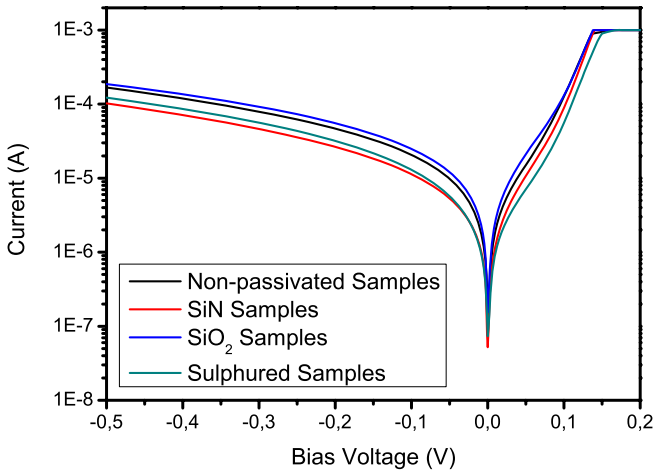

Figure 4.4: Dark I-V curve of passivated and O_2 plasma treated 400x400 μm^2 samples

For samples that are passivated with prior O_2 plasma treatment, dark current value is 20.65 μA for 400x400 μm^2 detectors at -100 mV bias, as shown in Fig. 4.4 and 4.5. With SiN_x passivation, this value is reduced to 11.32 μA. For SiO_2 passivation, the dark current is 24.83 μA for 400x400 μm^2 detectors at -100 mV bias, and sulphured solutions result in 12.97 μA dark current. Noting that the photocurrent due to room temperature radiation is 111.00 μA for 400x400 μm^2 detectors at a bias of -100 mV, SiN_x passivation with prior O_2 plasma treatment results in a photo current to dark current ratio of 10. We have 1.4 μA dark current for SiN_x passivated 200x200 μm^2 detectors; it is 100 nA for 100x100 μm^2 detectors, as shown in Fig. 4.6.

As seen from Fig.4.2, passivation in standard three solvent cleaned samples results in a decrease of the dark current by at least a factor of five times. This decrease

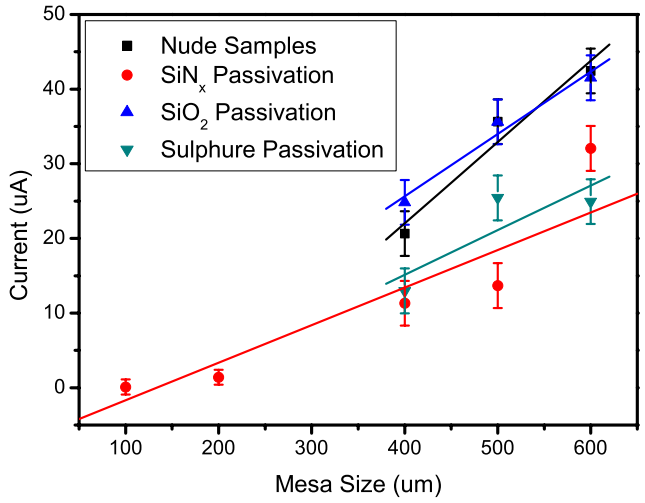

Figure 4.5: Dark current vs. mesa size of passivated samples with prior to O_2 plasma treatment at a bias of -100 mV (the lines are drawn to guide the eye)

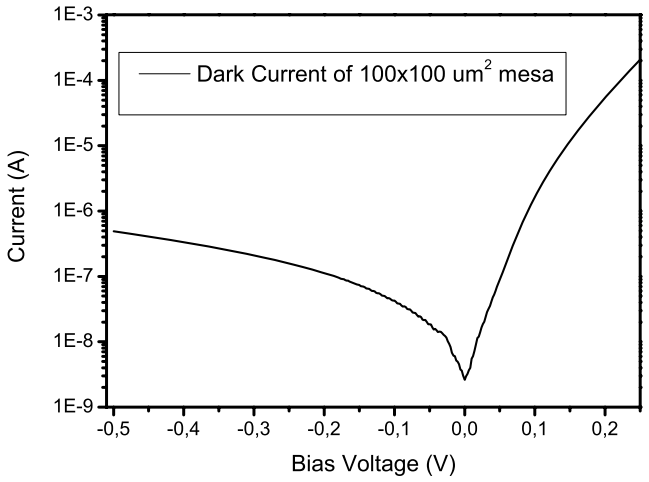

Figure 4.6: Dark I-V curve of SiN_x passivated and O_2 plasma treated sample with 100x100 μm^2 area

improves the S/N ratio. The best decrease in dark current is obtained with SiN_x passivation. Sulphure passivation seems to work well enough, however we observed that sulphur passivation degrades in time and results in an increase in dark current after twenty four hours in air, as seen in Fig.4.7, G. Beister et al, reports similar results [39] and also Hoffmann et al reports that sulphure destroys the surface by reacting with surface and passivated surface layers peel off [40]. In addition, application of sulphur passivation must be done under the fume-hood because the output H_2S gas is very hazardous, the decrease in dark current with sulphur passivation does not cover the damaging application and the degradation. G. Beister also reports that degradation in sulphur passivation can be minimized by a growth of SiN_x films onto sulphur passivated surfaces [39]. However our results with SiN_x passivation without sulphure pretreatment are better than those after sulphure treatment. In O_2 plasma treated samples, SiO_2 passivation after O_2 plasma treatments shows nearly no improvement in dark current. This means, we believe that, O_2 plasma does the job of SiO_2 passivation. Considering that application of O_2 plasma is a surface process that takes place in a very thin layer on the surface, we can conclude that saturation of the dangling bonds is enough for reduction of leakage current. We note that, in samples passivated with SiN_x or sulphure passivation with prior O_2 plasma treatment have resulted in at least two times improvement. A microscope image of various process steps of passivated samples are shown in Fig. 4.8

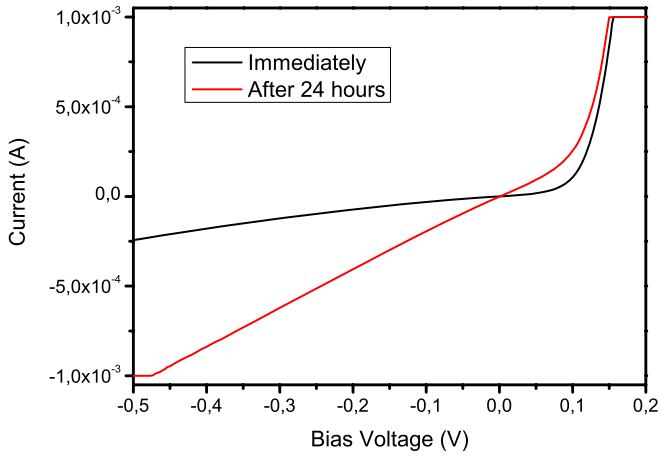

Figure 4.7: Degradation of dark current after sulphur passivation

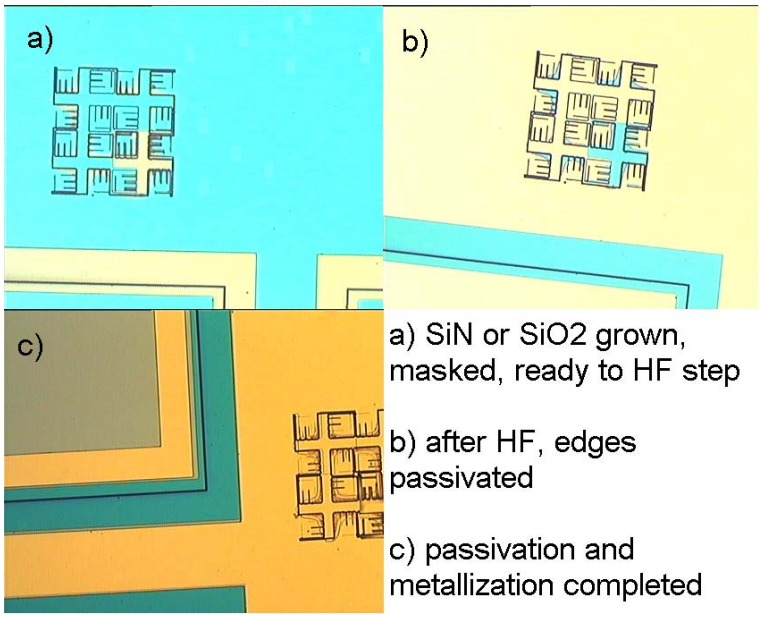

Figure 4.8: Microscope pictures of various process steps in passivated samples

Chapter 5

Conclusions and Future Work

5.1 Conclusions

InSb p-i-n photo detectors with different mesa sizes are designed and fabricated. Dark current of 140.00 μA is achieved for standard fabrication process at a bias of -100 mV for 400x400 μm^2 detectors averaged over at least 10 measurements. To reduce dark current, different treatments and passivation techniques are investigated. O_2 plasma cleaning after mesa etching process is found to be a reasonable way to reduce dark current and which has not been reported before in the literature. Dark current of a 400x400 μm^2 detector with O_2 plasma treatment is 20.65 μA at a bias of -100 mV, which indicates a decrease of 7 times in dark current. Depositing thin films of SiO_2 and SiN_x onto the sidewalls of the mesas reduced the dark current most for all mesa sizes by eliminating the surface states along the sidewalls of the detectors. Passivating the sidewalls with SiN_x and prior O_2 plasma treatment results in a decrease of two times in dark current, and it is 11.32 μA for the 400x400 μm^2 detectors. SiO_2 passivation reduced the dark current 15.55 μA from 140 μA. In general, SiO_2 passivation showed no reduction in dark current on samples with prior O_2 plasma treatment. We believe that, O_2 plasma does the job of SiO_2 passivation, this result is also not reported before. It may be helpful to note that if only SiO_2 passivation is to be used, O_2

plasma treatment can save one from dealing with HF and another lithography step. In addition, we tried aqua passivation techniques like sulphured solutions. Sulphure passivation works and we observed a decrease in dark current by at least five but it destroys the surface of detector [SEM picture available in [40]] and so it is not a good passivation choice for a robust operation. The reported values above are the average values of at least 10 detectors; the best reduction, we achieved is by a factor of fifty on one of 500x500 μm^2 detectors. In general, O_2 plasma treatment after mesa etching and SiN_x passivation along the sidewalls of the detectors results in a decrease of at least 10 times in dark current. In the literature, Kimukin et al. reports 8 μA dark current for SiN_x passivated 150x150 μm^2 detectors at -100 mV bias [41]. Besikci et al. reports 13 μA dark current for SiNx passivated 400x80 μm^2 detectors at same bias [3]. As a comparison, our 200x200 μm^2 detectors have 1.4 μA dark current with SiN_x passivation and with prior O_2 plasma treatment, and a dark current value below 13 μA for 400x400 μm^2 detectors. As a conclusion of our work we can state that, the best way of fabricating InSb photo detectors with low dark currents is applying O2 plasma after every photo resist removal step and using SiN_x for passivation.

5.2 Future Work

In the future, other materials such as BCB [42], SU8 [43], and polyimide [44] can be tried for passivation of InSb infrared detectors. Polyimides are very good insulators, and it is hoped that polyimide passivation will help to reduce dark currents to the order of tens of nano amperes at -0.1 V bias.

Bibliography

[1] E. J. Johnson. *Semiconductor and Semimetals*, volume 3. Academic, New York, 1967.

[2] G. W. Gobeli and H. Y. Fan. Infrared absorption and valence band in indium antimonide. *Phys. Rev.*, 119(2):613–620, Jul 1960.

[3] Tevke A. Insb infrared p-i-n photodetectors grown on gaas coated si substrates by molecular beam epitaxy. *Solid-State Electronics*, 42:1039–1044(6), June 1998.

[4] William Herschel. Experiments on the refrangibility of the invisible rays of the sun. by william herschel, ll. d. f. r. s. *Philosophical Transactions of the Royal Society of London*, 90:284–292, 1800.

[5] E. Barr. The infrared pioneers - III. Samuel Pierpont Langley. *Infrared Physics*, 3:195–196, December 1963.

[6] T. W. Case. Notes on the change of resistance of certain substrates in light. *Phys. Rev.*, 9:305–310, 1917.

[7] Gert Finger, James Garnett, Naidu Bezawada, Reinhold Dorn, Leander Mehrgan, Manfred Meyer, Alan Moorwood, J?rg Stegmeier, and Guy Woodhouse. Performance evaluation and calibration issues of large format infrared hybrid active pixel sensors used for ground- and space-based astronomy. *Nuclear Instruments and Methods in Physics Research Section A: Accelerators, Spectrometers, Detectors and Associated Equipment*, 565(1):241 – 250, 2006.

Proceedings of the International Workshop on Semiconductor Pixel Detectors for Particles and Imaging - PIXEL 2005.

[8] A. Rogalski, J. Antoszewski, and L. Faraone. Third-generation infrared photodetector arrays. *JOURNAL OF APPLIED PHYSICS*, 105(9), MAY 1 2009.

[9] Philippe Tribolet, Sophie Blondel, Patricia Costa, Agnes Combette, Laurent Vial, Gerard Destefanis, Philippe Ballet, Jean Paul Zanatta, Olivier Gravrand, Christophe Largeron, Jean Paul Chamonal, and Alain Million. Mwir focal plane arrays made with hgcdte grown by mbe on germanium substrates. volume 6206, page 62062F. SPIE, 2006.

[10] J. D. Vincent. *Fundamentals of Infrared Detector Operation and Testing*. February 1990.

[11] S. D. Gunapala, S. V. Bandara, J. K. Liu, C. J. Hill, S. B. Rafol, J. M. Mumolo, J. T. Trinh, M. Z. Tidrow, and P. D. LeVan. 1024x1024 pixel mwir and lwir qwip focal plane arrays and 320x256 mwir:lwir pixel colocated simultaneous dualband qwip focal plane arrays (invited paper). volume 5783, pages 789–803. SPIE, 2005.

[12] A. Rogalski, J. Antoszewski, and L. Faraone. Third-generation infrared photodetector arrays. *Journal of Applied Physics*, 105(9):091101, 2009.

[13] S. M. SZE. *Physics of Semiconductor Devices*. Wiley-Interscience, September, 1981.

[14] Akio Sasaki, Masahiro Nishiuma, and Yoshikazu Takeda. Energy band structure and lattice constant chart of iii-v mixed semiconductors, and algasb/algaassb semiconductor lasers on gasb substrates. *Japanese Journal of Applied Physics*, 19(9):1695–1702, 1980.

[15] C. L. Littler and D. G. Seiler. Temperature dependence of the energy gap of insb using nonlinear optical techniques. *Applied Physics Letters*, 46(10):986–988, 1985.

[16] Antoni Rogalski. Infrared detectors: an overview. *Infrared Physics and Technology*, 43(3-5):187 – 210, 2002.

[17] Edson G.; Kawakami Yoshifumi; Moriyasu Yoshitaka ; Nagase Kazuhiro; Kuze Naohiro Ueno, Koichiro; Camargo. A novel InSb photodiode infrared sensor operating at room temperature. 2006.

[18] P. W. Kruse. *Semiconductor and Semimetals*, volume 5. Academic, New York, 1970.

[19] Donald N. B. Hall, Richard S. Aikens, Richard Joyce, and Thomas W. McCurnin. Johnson noise limited operation of photovoltaic insb detectors. *Appl. Opt.*, 14(2):450–453, 1975.

[20] Lior Shkedy, Ornit Amir, Zipora Calahora, Joelle Oiknine-Schlesinger, and Igor Szafranek. Temperature dependence of spatial noise in insb focal plane arrays. volume 4028, pages 481–488. SPIE, 2000.

[21] Evangelos Theocharous. Stability of the spectral responsivity of cryogenically cooled insb infrared detectors. *Appl. Opt.*, 44(29):6087–6092, 2005.

[22] S. Forrest. Performance of inxga1-xasyp1-yphotodiodes with dark current limited by diffusion, generation recombination, and tunneling. *Quantum Electronics, IEEE Journal of*, 17(2):217 – 226, feb 1981.

[23] F. K. Hopkins and J. T. Boyd. Dark current analysis of insb photodiodes. *Infrared Physics*, 24(4):391 – 395, 1984.

[24] Bo-Liang Chen; Yueqing Zhang; Xiaoming Fang; Juncao Lin. Determination of hole diffusion length in n-insb at 80 k (proceedings paper). *Infrared Technology and Applications XXVII, Bjorn F. Andresen; Gabor F. Fulop; Marija Strojnik, Editors, pp.436-440*, 10 October 2001.

[25] I. Bloom and Y. Nemirovsky. Bulk lifetime determination of etch-thinned InSb wafers for two-dimensional infrared focal plane array. *IEEE Transactions on Electron Devices*, 39:809–812, April 1992.

[26] R. A. Laff and H. Y. Fan. Carrier lifetime in indium antimonide. *Phys. Rev.*, 121(1):53–62, Jan 1961.

[27] L. K. Li, Y. Hsu, and W. I. Wang. Molecular-beam epitaxial growth of insb on gaas and si for infrared detector applications. volume 11, pages 872–874. AVS, 1993.

[28] Kow-Ming Chang, Jiunn-Jye Luo, Cheng-Der Chiang, and Kou-Chen Liu. Wet etching characterization of insb for thermal imaging applications. *Japanese Journal of Applied Physics*, 45(3A):1477–1482, 2006.

[29] E. Michel, J. Xu, J.D. Kim, I. Ferguson, and M. Razeghi. Insb infrared photodetectors on si substrates grown by molecular beam epitaxy. *Photonics Technology Letters, IEEE*, 8(5):673 –675, may 1996.

[30] P. K. Maurya and P. Chakrabarti. Modeling and simulation of heterojunction photovoltaic detector based on InAs0 Sb-.15(0.85) for free space optical communication. *JOURNAL OF MATERIALS SCIENCE-MATERIALS IN ELECTRONICS*, 20(Suppl. 1):359–362, JAN 2009. 2nd International Conference on Optical and Optoelectronic Properties of Materials and Applications, London, ENGLAND, JUL 30-AUG 03, 2007.

[31] S. Maniv. volume 819, page 103. SPIE, 1987.

[32] Dr. S. Eker. *Private communications*. METU, Electric and Electronics Engineering.

[33] Elena Plis. *Mid-IR Type-II InAs-GaSb Nanoscale Superlattice Sensors*. PhD thesis.

[34] R. Adar, Y. Nemirovsky, and I. Kidron. Bulk tunneling contribution to the reverse breakdown characteristics of insb gate controlled diodes. *Solid-State Electronics*, 30(12):1289 – 1293, 1987.

[35] R. D. Baertsch. Noise and multiplication measurements in insb avalanche photodiodes. *Journal of Applied Physics*, 38(11):4267–4274, 1967.

[36] H. Simchi, Gh. Sareminia, A. Shafiekhani, and Gh. Valizadeh. Passivation of insb surface for manufacturing infrared devices. *Infrared Physics and Technology*, 51(3):263 – 269, 2008.

[37] X. Y. Gong, T. Yamaguchi, H. Kan, T. Makino, K. Ohshimo, M. Aoyama, M. Kumagawa, N. L. Rowell, and R. Rinfret. Sulphur passivation of inas(sb). *Applied Surface Science*, 113-114:388 – 392, 1997. Proceedings of the Eighth International Conference on Solid Films and Surfaces.

[38] D Sheela and Nandita DasGupta. Optimization of surface passivation for ingaas/inp pin photodetectors using ammonium sulfide. *Semiconductor Science and Technology*, 23(3):035018, 2008.

[39] G. Beister, J. Maege, J. Sebastian, G. Erbert, L. Weixelbaum, M. Weyers, J. Wurfl, and O.P. Daga. Stability of sulfur-passivated facets of ingaas-algaas laser diodes. *Photonics Technology Letters, IEEE*, 8(9):1124 –1126, sept. 1996.

[40] J Hoffmann, T Lehnert, D Hoffmann, and H Fouckhardt. Advantages and disadvantages of sulfur passivation of inas/gasb superlattice waveguide photodiodes. *Semiconductor Science and Technology*, 24(6):065008, 2009.

[41] I. Kimukin, N. Biyikli, T. Kartaloglu, O. Aytur, and E. Ozbay. High-speed insb photodetectors on gaas for mid-ir applications. *Selected Topics in Quantum Electronics, IEEE Journal of*, 10(4):766 – 770, july-aug. 2004.

[42] H.S. Kim, J.H. Choi, H.M. Bang, Y. Jee, S.W. Yun, J. Burm, M.D. Kim, and A.G. Choo. Dark current reduction in apd with bcb passivation. *Electronics Letters*, 37(7):455 –457, 29 2001.

[43] H. S. Kim, E. Plis, N. Gautam, A. Khoshakhlagh, S. Myers, M. N. Kutty, Y. Sharma, L. R. Dawson, and S. Krishna. Su-8 passivation of type-ii inas/gasb strained layer superlattice detectors. volume 7660, page 76601U. SPIE, 2010.

[44] D Sheela and Nandita DasGupta. Optimization of surface passivation for ingaas/inp pin photodetectors using ammonium sulfide. *Semiconductor Science and Technology*, 23(3):035018, 2008.

Appendix A

Fabrication Processes

1. Cleanroom procedure
   (a) Class 100 customs
      i. Always wear mask and glasses
      ii. Use separate beakers for separate purposes
      iii. Never lend your beakers and tweezers to anyone else
      iv. Keep clean beakers after using
      v. Clean your tweezers in soft cleaning step with sample
      vi. Always use tweezers inclined as bottom of tweezers is at the bottom to keep head of the tweezers clean
      vii. Keep in mind that "keep everything clean so you do not have to clean"
2. Cleaning
   (a) Hard cleaning
      i. Place sample on 5 pieces cleanroom tissues
      ii. Place a lens cleaning tissue on sample
      iii. Pour ace drops on sample
      iv. Gently pull lens tissue horizontally w/o moving sample
      v. Do it 3-5 times (no same spot on tissue twice)

vi. Use meth with a new lens tissue

vii. Do it 3-5 times

viii. Do not use iso

ix. Take a picture of sample

x. Soft cleaning required after operation

(b) Soft cleaning

i. Hot ace (5 min, 120 ^oC) (put tweezers in beaker to prevent explosion)

ii. Cold meth (5 min)

iii. Hot iso (5 min, 150 ^oC) (put tweezers in beaker to prevent explosion)

iv. Cold di water (3 min)

v. Rinse in di water (2 min)

vi. Blow dry with N_2

vii. Take a picture of sample

viii. Dehydration bake (min. 10 min, 120 ^oC)

(c) Equipment cleaning

i. Before use any acid or acidic solution, know which acid reacts with which things

ii. Prepare any solution on the wet bench, under the hood

iii. Never pour water onto acids

iv. Be present when cleaning

v. When done, dilute the solution first

vi. Pour the solution to the sink and pour water a while

3. Pre-lithography

(a) Spinning

i. Wait for pr to cool down to room temperature

ii. Pour pr on sample (no empty spots and bubbles)

iii. If mesas are present and depth is more than 1.5 micron, try to planarize the pr on the surface

iv. To do that, spin pr slowly or use another pr which is thicker than AZ5214E

v. Spin at 2 step mode

A. 500 rpm for 5 sec

B. 5000 rpm for 45 sec

vi. Pre-bake (110^oC for 1 min)

vii. Wait sample to cool down

viii. Ready for lithography

4. Lithography

(a) Adjusting

i. First adjust x-y roughly

ii. Start adjusting z depth

iii. Then go on iterations

iv. Watch sample edges, when sample touches mask you should see the wave pattern

v. Ready to launch

(b) UV Exposure

i. AZ5214E needs at least 270 mJ/cm^2

ii. For quartz masks, approx. 45-60 sec

iii. For soda lime masks, approx. 90-120 sec

(c) Develop

i. Dip sample into toluene if needed

ii. Blow dry with N_2 for toluene step

iii. Prepare AZ400K:DI water (1:4)

iv. Dip sample in developer

v. Try to keep sample horizontal

vi. Watch sample for changes

vii. Depend on excess exposure time, it should take 20-45 secs to develop

viii. Rinse in DI water for 1 min

ix. Blow dry with N_2

x. Take a picture of sample

5. Pre-etch

   (a) Post-bake

      i. Bake for 10 min @ 120 ^oC

      ii. Wait for sample to cool down

   (b) Cleaning residue photoresist

      i. O_2 plasma for 30 sec

      ii. To remove oxide, dip sample into ammonium hydroxide

      iii. Rinse in DI water

      iv. Blow dry with N_2

6. Mesa fabrication

   (a) Solution preparation

      i. Mix citric acid monohydrate:DI water (1:1)

      ii. Bake @ 90 ^oC, (endothermic reaction)

      iii. Keep stirring until no particle exists

      iv. Filter the solution if you want

      v. Wait 30 min to cool down

      vi. Add H_2O_2 - solution:H_2O_2 (50:1)

      vii. Heat solution for fast etching

   (b) Etching

      i. Put sample into solution

      ii. Keep sample horizontal

      iii. Shake for 1 min to etch go uniform

      iv. Get sample off the beaker to measure depth

v. Rinse in di water

vi. Blow dry with N_2

vii. Measure the depth at dektak station

viii. Put sample into solution if depth is not enough

ix. Put sample into ace if depth is satisfied

x. Apply soft cleaning

xi. Take a picture of sample

7. Metallization

(a) Preparation

i. Use toluene in the lithography step if needed

ii. Change box coater's pedestals

iii. Use clean boats

iv. Put a little ti onto boats

v. Put 0.3 gr gold for 100 nm thickness

vi. Vacuum chamber for an hour

vii. Check vacuum, it should at least 1e-6 Torr

viii. Setup the program

(b) Evaporation

i. This step should be short in time as possible, and sample should not be heated much. Thus adjust power accordingly.

ii. When deposition starts, switch manual mode and increase power fast up to a certain value. This is because in automatic mode, program increases power slowly so time gets longer. Thus pr gets heat.

iii. Use 1-2 a/sec rate for ti

iv. Use 10 a/sec rate for gold

v. After evaporation wait 1-2 min to vacuum gas inside the chamber

vi. Break the vacuum

vii. Take out your sample

(c) Liftoff

i. Put sample into ace

ii. Wait overnight if you have time

iii. Squirt ace on sample if metal did not liftoff

iv. Try ultrasonic vibrater if metal did not liftoff, be aware that this step may break and make dirty your sample

v. Apply soft cleaning

vi. Take a picture of sample